DOI: 10.13009/EUCASS2017-691

7TH EUROPEAN CONFERENCE FOR AERONAUTICS AND AEROSPACE SCIENCES (EUCASS)

DOI: ADD DOINUMBER HERE

Numerical study of acoustic radiation effects on air-assisted jets

N. Rutard[⋆], *L.-H. Dorey*[⋆], *C. Le Touze*[⋆], *M. Théron*[⋆⋆] *and S. Ducruix*[†]
[⋆] ONERA- *The French Aerospace Lab*
F-92322 Châtillon, France
luc-henry.dorey@onera.fr
[⋆⋆] CNES *DLA*
F-75612 Paris Cedex, France
[†] *Laboratoire EM2C, CNRS, CentraleSupélec, Université Paris-Saclay*
F-92290 Châtenay-Malabry, France

3-6 July 2017

Abstract

The present work is motivated by the high-frequency combustion instabilities often encountered during liquid rocket engine developments. These instabilities are usually associated with transverse acoustic modes of the combustion chamber. In this framework, the objective of the present contribution is to gain comprehension on the dynamical response of coaxial two-phase flows submitted to transverse acoustic modulations. A formulation for the analytical acoustic radiation force experienced by a sphere submitted to a multi-harmonic stationary wave is first proposed. This formulation is then used as a reference to validate a compressible simulation code through a simple numerical case representative of what is experienced by the central liquid core in coaxial jets. Afterwards, the dynamics of a spray under acoustic radiation modulations are examined. It is found that the acoustic radiation force and the drag between the spray droplets and the gaseous phase play an important role in the size segregation mechanism. This last process may impact the triggering of combustion instabilities in liquid rocket engines at subcritical operating conditions.

1. Introduction

Understanding High-Frequency (HF) combustion instabilities in Liquid Rocket Engines (LRE) has been a significant matter since the second half of the twentieth century[1,8,14]. Indeed, high power densities and mean pressure involved in such engines (around 50 to 100 $\mathrm{GW \cdot m^{-3}}$ and 100 bar respectively) make this kind of combustion instabilities a dangerous phenomenon. Acoustic pressure oscillations due to the unsteady heat release of flames can rise up to 10 % of the mean pressure in the combustion chamber and may result in a dramatic increase of heat fluxes at chamber walls, causing damages to the propulsion system and possibly its destruction. Up to now, full-scale engine tests have been favoured for the study of combustion instabilities, as during the F1 program, between 1962 and 1966, for which more than 2 000 tests[24] have been carried out on first-stage Saturn V engines. However, the significant cost of full-scale tests incites the scientific community to explore other methods such as high-performance Large Eddy Simulations (LES) to give a better insight into triggering and coupling mechanisms of HF combustion instabilities.

Several LES studies of self-excited or forced instabilities in LRE can be found in the literature. Unsteady numerical simulations have been carried out to investigate the response of an isolated cryogenic flame submitted to a transverse acoustic modulation and determine the effect of the modulation frequency on both the central dense core and the flame itself[12]. To take into account a possible coupling effect between multiple flames as in full-size LRE, LES of the reduced-size test bench MASCOTTE[30] have been carried out[13] with 5 shear coaxial injectors. Furthermore, to get a better insight into the triggering of self-excited transverse instabilities, LES of the BKD test bench, comprising 42 shear coaxial injectors, have also been performed[29]. One may note that all these studies were carried out considering only transcritical conditions, which means that the combustion chamber operates at a mean pressure above the critical pressure of oxygen (p_{cr,O_2} = 50,4 bar) but with an injection temperature well below the critical value (T_{cr,O_2} = 155 K). To the best of the authors' knowledge, no similar numerical study has been presented yet in the literature considering

DOI: 10.13009/EUCASS2017-691

subcritical conditions. Because of numerous differences between mechanisms at stake in both kinds of operating conditions, the results obtained in transcritical cases cannot be extended to subcritical ones, which justifies the present work.

Contrary to transcritical conditions mentioned previously, in subcritical conditions the mean pressure in the combustion chamber is below the critical pressure of oxygen used as propellant. This kind of situation is observed during the engine ignition, when the pressure in the combustion chamber is arising from ambient pressure to its nominal value, and at low thrust operating conditions. The oxygen is then injected in the chamber in a liquid state, surrounded by a coaxial gaseous flow of fuel. Therefore, in opposition to transcritical conditions, a physical interface exists between both propellants and surface tension cannot be neglected. The central liquid core then undergoes primary atomization under the action of shear stresses. Small ligaments torn away from the liquid core experiment secondary fragmentation, thereby creating smaller quasi-spherical droplets. Finally, the presence of hot burn gases induces the liquid vaporisation which is crucial for combustion. All these mechanisms, inherent to subcritical conditions, may participate to the thermo-acoustic coupling. That is why it is absolutely necessary to reproduce them correctly when dealing with unsteady numerical simulations of subcritical cryogenic flames. One of the most challenging issues in simulating this kind of flow for a reasonable cost is to accurately describe all the liquid structures, from large separated two-phase flow down to the smaller droplets of the spray. To this end, a numerical strategy has been developed at Onera[19] for the coupling of a diffuse interface method adapted to the simulation of *separated phase* zones, and a Eulerian statistical model adapted to the simulation of sprays. This methodology has been applied to the LES of an isolated cryogenic LOX/GH_2 flame reproducing a subcritical operating point of the Mascotte test bench[20]. This numerical simulation demonstrated the great potential of this original strategy and justifies its use for numerical studies of HF combustion instabilities in subcritical conditions.

As mentioned before, multiple coupling mechanisms may intervene between acoustics, combustion and the coaxial stream in such combustion instabilities. As a first step of our study, it has been preferred to isolate acoustics / two-phase flow coupling mechanisms from combustion processes. Therefore, it is of great interest to review experimental studies on acoustic effects on non-reactive two-phase flows. Only transverse acoustic perturbations will be considered because these are known as the most destructive ones in LRE when coupling with combustion[8]. Experiments have first demonstrated the ability of intense acoustic perturbations to deviate round liquid jets at the acoustic frequency[5,6,23]. The same observation has been made later for coaxial jets[7,9,10], more representative of LRE's operating conditions. The second effect of acoustics being noticed has been a dramatic flattening of coaxial jets[15] under the action of transverse acoustic waves, this observation being confirmed later for round jets[6]. The authors explained these two phenomena by the presence of intense velocity fluctuations around the liquid core due to acoustics. More recent experiments of transverse acoustic perturbations applied to coaxial air/water flows[3,4,11] tend to agree with previous observations for a large range of atomization regimes. However, these physical phenomena are not only due to strong velocity fluctuations but also to the presence of acoustic radiation pressure[3]. This mechanism has been studied by King[16] in 1934 and can be viewed as a non-zero mean pressure variation in acoustic field. Usually mentioned as a non-linear effect, King proved that acoustic radiation pressure can also exist in linear acoustics, particularly around any object submitted to propagative or standing waves. In the case of two-phase flows submitted to transverse acoustic perturbations, the non-homogeneous pressure radiation profile around coaxial jets induces a suction effect and the flattening of the liquid core as soon as acoustic waves are intense enough to counterbalance the stabilizing effect of surface tension. In an equivalent way, spray droplets submitted to a non-symmetrical pressure radiation profile can experience a specific force causing their deviation.

At this point it is worth noting that in the case of reactive flows, all these interactions between acoustics and two-phase flows may play an important part in the setting of combustion instabilities in LRE. Therefore, the present paper aims at progressively evaluating the ability of a compressible simulation code to quantitatively reproduce acoustic radiation pressure and its previously mentioned effects on coaxial jets. First, a new formulation of the analytical acoustic radiation force experienced by a sphere submitted to a transverse standing wave is proposed, based on the initial model derived by King[16]. This formulation, described in section 2, brings the possibility to take into account linear and non-linear interactions between all harmonics contained in intense acoustic waves such as the ones that intervene in LRE at unstable operating points[8]. After a brief description of the Cedre code in section 3, this new formulation is used in section 4 as a reference to validate the code through a simple numerical case of a small rigid sphere submitted to a transverse acoustic modulation, representative of what is experienced by the central liquid core in coaxial jets. Afterwards, the spray behaviour under acoustic radiation forces is examined by simulating a polydisperse spray injected in a moving stream submitted to transverse acoustic modulations, which corresponds quite well to what happens downstream atomization processes in coaxial two-phase flows.

DOI: 10.13009/EUCASS2017-691

2. Acoustic radiation force on spheres in multi-harmonic standing waves

2.1 Analytical derivation

King[16] formulated the analytical expression of the mean acoustic radiation force applied to a sphere submitted to plane propagative or standing waves. In this model, the compressibility of the sphere and the viscosity of the medium are both neglected. In particular, King proposed a simplification of the expression when $\alpha = ka \ll 1$, where a is the sphere radius and k is the acoustic wave number defined as $k = 2\pi f/c$ with f the acoustic frequency and c the speed of sound in the medium. In this case, the appropriate expression for the temporal mean acoustic radiation force $\langle F_{rad}\rangle_{King}$ is:

$$\langle F_{rad}\rangle_{King} = -\pi\rho_0 A^2\alpha^3 \sin(2kh)\frac{1+\frac{2}{3}\left(1-\frac{\rho_0}{\rho_1}\right)}{2+\frac{\rho_0}{\rho_1}} f_{cor}\,, \tag{1}$$

where ρ_0 and ρ_1 are the medium and sphere densities respectively, $A = P_{ac}/(\rho_0 ck)$ with P_{ac} the acoustic amplitude, and $h = (x_{pan} - x)$ is the distance between a pressure anti-node x_{pan} and the centre of the sphere x. In cases where $\alpha \ll 1$ cannot be assumed, some authors[18,22] proposed the corrective factor $f_{cor}(\alpha) = 3/(4\alpha^2)\ [\sin(2\alpha)/(2\alpha) - cos(2\alpha)]$ tending to 1 for small spheres. Through this analytical model, King[16] demonstrated the part played by the acoustic radiation pressure on dust striations in resonance tubes and standing waves, as noticed by experimental investigation of acoustic effects on coaxial jets mentioned in section 1. However, in his work, the author made the hypothesis of mono-harmonic acoustic perturbations. But high acoustic levels can be reached in LRE in unsteady operating conditions, leading to acoustic non-linearities characterised by the presence of multiple harmonics. Therefore, it is of great interest to take into account the effect of these harmonics on the acoustic radiation force. To do so, a new formulation of King's model is derived below.

If we apply the equations of motion and continuity to an irrotational flow with constant speed of sound c, it is possible to write the pressure variation δp in the medium and the medium velocity components (u, v, w) as:

$$\delta p = p - p_0 = \rho_0\dot{\phi} - \frac{\rho_0}{2}q^2 + \frac{\rho_0}{2c^2}\dot{\phi}^2\,, \tag{2}$$

$$u = -\frac{\partial\phi}{\partial x}\ ;\ v = -\frac{\partial\phi}{\partial y}\ ;\ w = -\frac{\partial\phi}{\partial z}\,, \tag{3}$$

with p_0 the mean pressure in the medium, $\dot{\phi}$ the partial temporal derivative of the velocity potential ϕ and $q^2 = u^2 + v^2 + w^2$. As in King's work, the motion of the sphere under acoustics has to be considered. In the case of an acoustic field with radial symmetry with respect to the sphere, this one will be moving at velocity $\dot{\xi}$. With the material derivative $D\phi/Dt$ applied to the centre of the sphere, we can then write in spherical coordinates (r,θ,φ):

$$\dot{\phi} = \frac{D\phi}{Dt} - \dot{\xi}\cos\theta\frac{\partial\phi}{\partial r} + \dot{\xi}\frac{\sin\theta}{r}\frac{\partial\phi}{\partial\theta}\,. \tag{4}$$

Finally, the dynamical equation of motion of the sphere of mass $M = 4/3\pi a^3\rho_1$ and its corresponding boundary condition can be expressed as in equations (5) and (6), with $\mu = \cos\theta$:

$$2\pi a^2\int_{-1}^{1}\delta p\,\mu\,d\mu = M\ddot{\xi}\,, \tag{5}$$

$$-\frac{\partial\phi}{\partial r}_{|r=a} = \dot{\xi}\mu\,. \tag{6}$$

Let us now consider a standing wave composed of m harmonics. As in all acoustic problems, the velocity potential is a solution of the well-known wave equation. Thanks to the linear aspect of this equation, it is possible to decompose the total velocity potential of the multi-harmonic acoustic field ϕ into a sum of the velocity potentials of each isolated harmonic ϕ_i. By extending King's work to multi-harmonic standing waves, this can be expressed as:

$$\phi = \sum_{i=1}^{m}\phi_i\,, \tag{7}$$

$$\phi_i = \cos(\omega_i t + \psi_i)\sum_{n=0}^{\infty}(R_n(\alpha_i)P_n(\mu)) + \sin(\omega_i t + \psi_i)\sum_{n=0}^{\infty}(S_n(\alpha_i)P_n(\mu))\,, \tag{8}$$

DOI: 10.13009/EUCASS2017-691

where $\omega_i = 2\pi f_i$ with f_i the frequency of the i^{th} harmonic, ψ_i its phase and $P_n(\mu)$ the n^{th} - degree Legendre polynomial. For the sake of readability, the term $\omega_i t + \psi_i$ will be written Φ_i. In equation (7), ϕ is defined with respect to the moving origin centred on the sphere. The definitions of $R_n(\alpha_i)$ and $S_n(\alpha_i)$ are given in the system of equations (9):

$$\begin{cases} R_n(\alpha_i) &= \dfrac{A_i}{H_n(\alpha_i)\,\alpha_i^{n+1}}\,(2n+1)\,\cos(k_i h_i + \frac{1}{2}n\pi)\dfrac{F_n(\alpha_i)}{H_n(\alpha_i)}\,, \\ S_n(\alpha_i) &= -\dfrac{A_i}{H_n(\alpha_i)\,\alpha_i^{n+1}}\,(2n+1)\,\cos(k_i h_i + \frac{1}{2}n\pi)\dfrac{G_n(\alpha_i)}{H_n(\alpha_i)}\,, \end{cases} \tag{9}$$

where $k_i = 2\pi\omega_i$, $A_i = P_{ac,i}/(\rho_0 c k_i)$ with $P_{ac,i}$ the acoustic amplitude of the i^{th} harmonic, $\alpha_i = k_i a$, and $h_i = (x_{pan,i} - x)$, $x_{pan,i}$ being the position of a pressure anti-node for the i^{th} harmonic. We also define:

$$\begin{cases} F_n(\alpha_i) &= \alpha_i^2\,\beta_{n+1}(\alpha_i) - n\,\beta_n(\alpha_i) \qquad \text{when} \quad n \neq 1\,, \\ F_1(\alpha_i) &= \alpha_i^2\,\beta_2(\alpha_i) - (1 - \frac{\rho_0}{\rho_1})\,\beta_1(\alpha_i)\,, \\ G_n(\alpha_i) &= \alpha_i^2\,\gamma_{n+1}(\alpha_i) - n\,\gamma_n(\alpha_i) \qquad \text{when} \quad n \neq 1\,, \\ G_1(\alpha_i) &= \alpha_i^2\,\gamma_2(\alpha_i) - (1 - \frac{\rho_0}{\rho_1})\,\gamma_1(\alpha_i)\,, \end{cases} \tag{10}$$

and

$$\begin{cases} \beta_n(\alpha_i) &= (-1)^n\,\alpha_i^{-n}\left(\dfrac{\pi}{2\alpha_i}\right)^{\frac{1}{2}} J_{-n-\frac{1}{2}}(\alpha_i)\,, \\ \gamma_n(\alpha_i) &= \alpha_i^{-n}\left(\dfrac{\pi}{2\alpha_i}\right)^{\frac{1}{2}} J_{n+\frac{1}{2}}(\alpha_i)\,, \end{cases} \tag{11}$$

with $J_n(\alpha_i)$ the n^{th} - degree Bessel function.

Now that ϕ is defined as a function of the velocity potential of each harmonic, it is possible to use equations (2) and (5) together to express the acoustic radiation force F_{rad} as:

$$\begin{cases} F_{rad} &= 2\pi a^2 \rho_0 \displaystyle\int_{-1}^{1} \left(\dot{\phi} - \tfrac{1}{2}q^2 + \tfrac{1}{2c^2}\dot{\phi}^2\right)\,\mu\,d\mu\,, \\ &= 2\pi a^2 \rho_0 \left(f_{lin} + f_q + f_\phi + f_\xi\right)\,, \end{cases} \tag{12}$$

The terms f_{lin}, f_q, f_ϕ and f_ξ of equation (12) are defined below.

Analytical expression for f_{lin}

The first term f_{lin} in equation (12) refers to the linear interaction between harmonics at the surface of the sphere. This term is first order and can be expressed as in equation (13):

$$\begin{aligned} f_{lin} = \int_{-1}^{1} \frac{D\phi}{Dt}\mu d\mu = &\int_{-1}^{1} \sum_{i=1}^{m} \omega_i \left[\cos\Phi_i \sum_{n=0}^{\infty}\left(S_n(\alpha_i)P_n(\mu)\right)\right]\mu d\mu \\ &- \int_{-1}^{1} \sum_{i=1}^{m} \omega_i \left[\sin\Phi_i \sum_{n=0}^{\infty}\left(R_n(\alpha_i)P_n(\mu)\right)\right]\mu d\mu\,. \end{aligned} \tag{13}$$

Thanks to the definition of Legendre polynomials, it can be proved that,

$$\int_{-1}^{1} P_n(\mu)P_m(\mu)d\mu = \begin{cases} \dfrac{2}{2n+1} & \text{when} \quad m = n\,, \\ 0 & \text{otherwise}\,. \end{cases} \tag{14}$$

As a result, since $P_1(\mu) = \mu$, we finally obtain equation (15):

$$f_{lin} = \frac{2}{3}\sum_{i=1}^{m} \omega_i \left[\cos\Phi_i\, S_1(\alpha_i) - \sin\Phi_i\, R_1(\alpha_i)\right]. \tag{15}$$

DOI: 10.13009/EUCASS2017-691

Analytical expression for f_q

The second term f_q in equation (12) is one of the three terms playing a part in second-order harmonic interactions. By using the definition of q^2 in spherical coordinates and the equation (6), we obtain:

$$\begin{aligned} f_q &= -\frac{1}{2}\int_{-1}^{1} q^2 \mu d\mu \,, \\ &= -\frac{1}{2}\int_{-1}^{1}\left[\dot{\xi}^2\mu^2 + \frac{1}{a^2}\left(\frac{\partial\phi}{\partial\mu}\right)^2\left(1-\mu^2\right)\right]\mu d\mu \,, \\ &= -\frac{1}{2\,a^2}\int_{-1}^{1}\left(\frac{\partial\phi}{\partial\mu}\right)^2\left(1-\mu^2\right)\mu d\mu \,. \end{aligned} \tag{16}$$

By using equations (7) and (8), the term $(\partial\phi/\partial\mu)^2$ in equation (16) can be written as:

$$\begin{aligned} \left(\frac{\partial\phi}{\partial\mu}\right)^2 = &\sum_{i=1}^{m}\left(\cos\Phi_i\sum_{n=0}^{\infty}\left(R_n(\alpha_i)\frac{\partial P_n}{\partial\mu}\right) + \sin\Phi_i\sum_{n=0}^{\infty}\left(S_n(\alpha_i)\frac{\partial P_n}{\partial\mu}\right)\right)^2 \\ &+ 2\sum_{1\le i<j\le m}\frac{\partial\phi_i}{\partial\mu}\frac{\partial\phi_j}{\partial\mu}\,. \end{aligned} \tag{17}$$

Thanks to the definition of Legendre polynomials, it can be proved that,

$$\int_{-1}^{1}\frac{\partial P_n}{\partial\mu}\frac{\partial P_m}{\partial\mu}(1-\mu^2)\mu d\mu = \begin{cases} \dfrac{2n(n+1)(n+2)}{(2n+1)(2n+3)} & \text{when} \quad m = n+1\,, \\ 0 & \text{otherwise}\,. \end{cases} \tag{18}$$

Finally, thanks to equations (16), (17) and (18), we can define $f_q = f_{q1} + f_{q2}$, with f_{q1} and f_{q2} respectively expressed as in equations (19) and (20):

$$\begin{aligned} f_{q1} = &-\frac{1}{2\,a^2}\sum_{i=1}^{m}\left[\cos^2\Phi_i\sum_{n=0}^{\infty}\frac{4n(n+1)(n+2)}{(2n+1)(2n+3)}R_n(\alpha_i)R_{n+1}(\alpha_i)\right] \\ &-\frac{1}{2\,a^2}\sum_{i=1}^{m}\left[\sin^2\Phi_i\sum_{n=0}^{\infty}\frac{4n(n+1)(n+2)}{(2n+1)(2n+3)}S_n(\alpha_i)S_{n+1}(\alpha_i)\right] \\ &-\frac{1}{2\,a^2}\sum_{i=1}^{m}\left[\cos\Phi_i\sin\Phi_i\sum_{n=0}^{\infty}\frac{4n(n+1)(n+2)}{(2n+1)(2n+3)}\left(R_n(\alpha_i)S_{n+1}(\alpha_i) + R_{n+1}(\alpha_i)S_n(\alpha_i)\right)\right], \end{aligned} \tag{19}$$

$$\begin{aligned} f_{q2} = &-\frac{1}{2\,a^2}\sum_{1\le i<j\le m}\left[\cos\Phi_i\cos\Phi_j\sum_{n=0}^{\infty}\frac{4n(n+1)(n+2)}{(2n+1)(2n+3)}\left(R_n(\alpha_i)R_{n+1}(\alpha_j) + R_{n+1}(\alpha_i)R_n(\alpha_j)\right)\right] \\ &-\frac{1}{2\,a^2}\sum_{1\le i<j\le m}\left[\sin\Phi_i\sin\Phi_j\sum_{n=0}^{\infty}\frac{4n(n+1)(n+2)}{(2n+1)(2n+3)}\left(S_n(\alpha_i)S_{n+1}(\alpha_j) + S_{n+1}(\alpha_i)S_n(\alpha_j)\right)\right] \\ &-\frac{1}{2\,a^2}\sum_{1\le i<j\le m}\left[\cos\Phi_i\sin\Phi_j\sum_{n=0}^{\infty}\frac{4n(n+1)(n+2)}{(2n+1)(2n+3)}\left(R_n(\alpha_i)S_{n+1}(\alpha_j) + R_{n+1}(\alpha_i)S_n(\alpha_j)\right)\right] \\ &-\frac{1}{2\,a^2}\sum_{1\le i<j\le m}\left[\cos\Phi_j\sin\Phi_i\sum_{n=0}^{\infty}\frac{4n(n+1)(n+2)}{(2n+1)(2n+3)}\left(R_n(\alpha_j)S_{n+1}(\alpha_i) + R_{n+1}(\alpha_j)S_n(\alpha_i)\right)\right]. \end{aligned} \tag{20}$$

Analytical expression for f_ϕ

The second term playing a part in harmonic interactions in equation (12) is f_ϕ. By using equation (7) and limiting

DOI: 10.13009/EUCASS2017-691

the expansion of $\dot{\phi}^2$ to second-order terms, we can write:

$$\begin{aligned} f_\phi &= \frac{1}{2\,c^2}\int_{-1}^{1}\dot{\phi}^2\mu d\mu\,, \\ &= \frac{1}{2\,c^2}\int_{-1}^{1}\left(\sum_{i=1}^{m}\left(\frac{D\phi_i}{Dt}\right)^2 + 2\sum_{1\le i<j\le m}\frac{D\phi_i}{Dt}\frac{D\phi_j}{Dt}\right)\mu d\mu\,, \\ &= f_{\phi 1} + f_{\phi 2}\,. \end{aligned} \tag{21}$$

Thanks to the definition of Legendre polynomials, it can be proved that,

$$\int_{-1}^{1} P_n(\mu)P_m(\mu)\mu d\mu = \begin{cases} \dfrac{2(n+1)}{(2n+1)(2n+3)} & \text{when} \quad m = n+1\,, \\ 0 & \text{otherwise}\,. \end{cases} \tag{22}$$

Therefore, we finally obtain equations (23) and (24) to express $f_{\phi 1}$ and $f_{\phi 2}$ respectively:

$$\begin{aligned} f_{\phi 1} &= \frac{1}{2\,c^2}\int_{-1}^{1}\sum_{i=1}^{m}\left(\frac{D\phi_i}{Dt}\right)^2\mu d\mu\,, \\ &= \sum_{i=1}^{m}\left[{k_i}^2\cos^2\Phi_i\sum_{n=0}^{\infty}\frac{2(n+1)}{(2n+1)(2n+3)}S_n(\alpha_i)S_{n+1}(\alpha_i)\right] \\ &+ \sum_{i=1}^{m}\left[{k_i}^2\sin^2\Phi_i\sum_{n=0}^{\infty}\frac{2(n+1)}{(2n+1)(2n+3)}R_n(\alpha_i)R_{n+1}(\alpha_i)\right] \\ &- \sum_{i=1}^{m}\left[{k_i}^2\cos\Phi_i\sin\Phi_i\sum_{n=0}^{\infty}\frac{2(n+1)}{(2n+1)(2n+3)}\Big(S_n(\alpha_i)R_{n+1}(\alpha_i) + S_{n+1}(\alpha_i)R_n(\alpha_i)\Big)\right], \end{aligned} \tag{23}$$

$$\begin{aligned} f_{\phi 2} &= \frac{1}{c^2}\int_{-1}^{1}\sum_{1\le i<j\le m}\frac{D\phi_i}{Dt}\frac{D\phi_j}{Dt}\mu d\mu\,, \\ &= \sum_{1\le i<j\le m}\left[k_i k_j\cos\Phi_i\cos\Phi_j\sum_{n=0}^{\infty}\frac{2(n+1)}{(2n+1)(2n+3)}\Big(S_n(\alpha_i)S_{n+1}(\alpha_j) + S_{n+1}(\alpha_i)S_n(\alpha_j)\Big)\right] \\ &+ \sum_{1\le i<j\le m}\left[k_i k_j\sin\Phi_i\sin\Phi_j\sum_{n=0}^{\infty}\frac{2(n+1)}{(2n+1)(2n+3)}\Big(R_n(\alpha_i)R_{n+1}(\alpha_j) + R_{n+1}(\alpha_i)R_n(\alpha_j)\Big)\right] \\ &- \sum_{1\le i<j\le m}\left[k_i k_j\cos\Phi_i\sin\Phi_j\sum_{n=0}^{\infty}\frac{2(n+1)}{(2n+1)(2n+3)}\Big(S_n(\alpha_i)R_{n+1}(\alpha_j) + S_{n+1}(\alpha_i)R_n(\alpha_j)\Big)\right] \\ &- \sum_{1\le i<j\le m}\left[k_j k_i\cos\Phi_j\sin\Phi_i\sum_{n=0}^{\infty}\frac{2(n+1)}{(2n+1)(2n+3)}\Big(S_n(\alpha_j)R_{n+1}(\alpha_i) + S_{n+1}(\alpha_j)R_n(\alpha_i)\Big)\right]. \end{aligned} \tag{24}$$

Analytical expression for f_ξ

The term f_ξ in equation (12) is the last term playing a part in harmonic interactions. This term has to be considered only when the sphere is free to move under the action of acoustics. By using the boundary condition (6), we obtain:

$$\begin{aligned} f_\xi &= \int_0^\pi\left(-\dot{\xi}\cos\theta\frac{\partial\phi}{\partial r} + \dot{\xi}\frac{\sin\theta}{a}\frac{\partial\phi}{\partial\theta}\right)\sin\theta\,\cos\theta\,d\theta\,, \\ &= \frac{\dot{\xi}}{a}\int_{-1}^{1}(\mu^2-1)\frac{\partial\phi}{\partial\mu}\mu d\mu\,. \end{aligned} \tag{25}$$

DOI: 10.13009/EUCASS2017-691

An integration by part together with the use of equation (14) lead to:

$$\begin{aligned} f_\xi &= -2\,\frac{\dot{\xi}}{a}\int_{-1}^{1}\left[P_2(\mu)\underbrace{\sum_{i=1}^{m}\left(\cos\Phi_i\sum_{n=0}^{\infty}\left(R_n(\alpha_i)P_n(\mu)\right)+\sin\Phi_i\sum_{n=0}^{\infty}\left(S_n(\alpha_i)P_n(\mu)\right)\right)}_{\phi}\right]d\mu\,, \\ &= -\frac{4}{5}\frac{\dot{\xi}}{a}\sum_{i=1}^{m}\Big(\cos\Phi_i R_2(\alpha_i)+\sin\Phi_i S_2(\alpha_i)\Big)\,. \end{aligned} \tag{26}$$

In order to determine the sphere velocity $\dot{\xi}$, it is sufficiently accurate to consider only first-order terms in equation (2). After integrating with respect to time, the dynamical equation becomes:

$$\begin{aligned} \dot{\xi} &\approx \frac{2\pi a^2\rho_0}{M}\int_{-1}^{1}\phi\,\mu\,d\mu\,, \\ &\approx \frac{1}{a}\frac{\rho_0}{\rho_1}\sum_{i=1}^{m}\Big(\cos\Phi_i R_1(\alpha_i)+\sin\Phi_i S_1(\alpha_i)\Big)\,. \end{aligned} \tag{27}$$

We finally obtain equation (28):

$$f_\xi = -\frac{4}{5}\frac{1}{a^2}\frac{\rho_0}{\rho_1}\sum_{i=1}^{m}\Big(\cos\Phi_i R_1(\alpha_i)+\sin\Phi_i S_1(\alpha_i)\Big)\sum_{i=1}^{m}\Big(\cos\Phi_i R_2(\alpha_i)+\sin\Phi_i S_2(\alpha_i)\Big)\,. \tag{28}$$

As a result, the acoustic radiation force experienced by a small sphere submitted to a multi-harmonic standing wave is formulated through equation (12) together with equations (15), (19), (20), (23), (24) and (28). Contrary to King's work[16], no time integration has been carried out. However, orders of magnitude of each term in F_{rad} can be estimated to show that the effect of temporal fluctuations of the acoustic radiation force on the sphere deviation can be neglected in most cases.

2.2 Discussion on temporal aspects

As shown previously, the acoustic radiation force can be defined as $F_{rad} = 2\pi a^2\rho_0\left(f_{lin}+f_q+f_\phi+f_\xi\right)$. Among these terms, it comes up that $\langle f_{lin}\rangle = 0$. The only terms playing a part in the temporal mean acoustic radiation force $\langle F_{rad}\rangle$ are then $\langle f_q\rangle$, $\langle f_\phi\rangle$ and $\langle f_\xi\rangle$. Moreover, it can be proved that the amplitude of f_{lin} is at least two orders of magnitude higher than the three others f_q, f_ϕ and f_ξ. From these observations, we can approximate F_{rad} as:

$$F_{rad} = \underbrace{2\,\pi\,a^2\,\rho_0\left(\langle f_q\rangle+\langle f_\phi\rangle+\langle f_\xi\rangle\right)}_{\langle F_{rad}\rangle} + \underbrace{2\,\pi\,a^2\,\rho_0\,f_{lin}}_{F'_{rad}(t)}\,. \tag{29}$$

For the sake of simplicity, only one harmonic will be considered in our approximation. In that case, and if $\alpha_i \ll 1$, $S_1(\alpha_i) \approx 0$ in equation (15). If we define C_1 as the amplitude of $F'_{rad}(t)$ and $C_2 = \langle F_{rad}\rangle$, equation (29) becomes $F_{rad} \approx -C_1\sin\Phi_i + C_2$. To approximate the order of magnitude of the displacement due to each term of F_{rad}, we can integrate the classical equation of motion with respect to time:

$$\begin{aligned} F_{rad} &= M\frac{\partial^2\xi}{\partial t^2}\,, \\ \rightarrow\ \xi &\approx \underbrace{\frac{C_1}{M\,\omega_i^2}}_{x_1}\sin\Phi_i + \underbrace{\frac{C_2}{2\,M}}_{x_2}\,t^2\,. \end{aligned} \tag{30}$$

Finally, by estimating C_1 and C_2 thanks to equations (15) and (1) respectively, we find the ratio between x_1 and x_2:

$$\frac{x_2}{x_1} \approx \frac{5}{6}\frac{P_{ac,i}}{\rho_0}\,{k_i}^2\,\cos(k_i\,h_i)\,. \tag{31}$$

If we apply this approximation to typical values encountered in LRE in subcritical operating conditions, we find a ratio rising up to 10^7 s^{-2}. Therefore, in such conditions, the sinusoidal displacement due to acoustic radiation force

DOI: 10.13009/EUCASS2017-691

fluctuations $F'_{rad}(t)$ becomes quickly negligible compared to the mean displacement, except for objects already located in velocity anti-nodes where $x_2 = 0$. As a conclusion, only the mean temporal values of the acoustic radiation force will be analysed in the next sections of this paper.

3. Numerical methods

3.1 Eulerian/Eulerian coupling strategy

Numerical simulations presented in this paper are performed with the Cedre industrial code[25] developed at Onera. Cedre is used for multi-physics simulations in energetics and propulsion and is based on the coupling of several solvers, each of them being dedicated to model specific physical phenomena. The code uses the finite volume method and can handle general unstructured meshes.

As previously mentioned, non-reactive air-assisted jets undergo successive atomization steps involving a wide range of scales. To correctly describe all of them, a numerical strategy has been developed at Onera[19] for the coupling of a diffuse interface method and a Eulerian statistical model, respectively integrated in Cedre solvers Charme and Spiree. This coupling strategy is represented in figure 1. A diffuse interface method referred to as "4-equation model" or "Locally Homogeneous Flow" (LHF)[19] is used to simulate the *separated phase* zones where liquid structures are fully described by the mesh while the Spiree solver is used to follow the spray (*dispersed phase* zone) in a statistical way as soon as the mesh becomes too coarse to describe the interface between the droplets ans the gas. This methodology does not enable us to take into account the *mixed zone* where liquid fragments torn from the central liquid core are too small to be described by the mesh and cannot be considered as being part of the spray yet. However, the impact of this zone on the spray behaviour is considered negligible in a first approach.

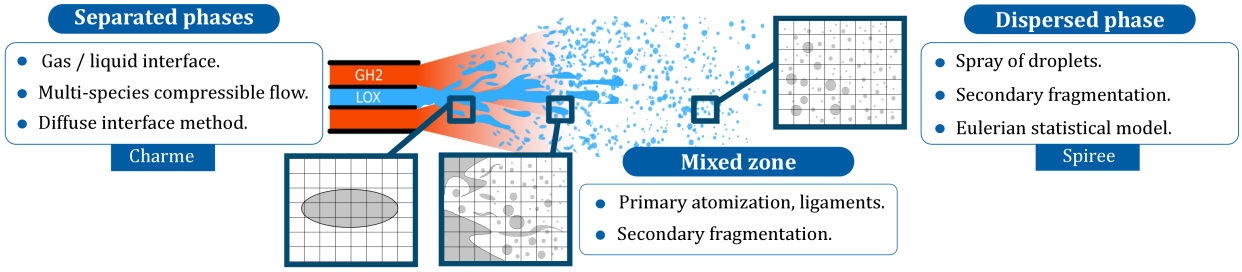

Figure 1: Coupling strategy for two-phase flow simulations from Cedre.

In the following sections of this paper, the dense liquid phase will not be simulated. As a first approach, the two-phase flow will then only be composed of a gaseous ambient flow and a liquid spray simulated thanks to the Charme and Spiree solvers respectively.

3.2 Charme solver

In the Charme solver, the gaseous flow is described by multi-species compressible Navier-Stokes equations with an LES formalism. The system closure is provided by the ideal gas law. Upwind numerical fluxes based on approximate Riemann solvers, such as the HLLC flux scheme[28], are used to approximate the convective fluxes. Second-order multislope MUSCL reconstructions extended to general unstructured grids[21] are computed on each grid faces. For the viscous terms, a central differencing method is used whereas the source terms are evaluated with the value of the variables at the cell centers. Finally, we use the three-step explicit Runge-Kutta scheme for time integration.

3.3 Spiree solver

In all generality, polydisperse sprays can be described by Williams statistical kinetic equation[31] on the Number Density Function (NDF). Direct resolution of this equation is nevertheless out of reach for practical applications. This is why in practice we perform a reduction of the highly-dimensional phase space by solving Eulerian transport equations on some moments of the NDF. To do so, the kinetic equation is integrated over droplets velocity $\boldsymbol{w}$ and temperature θ, leading to a semi-kinetic system[17,26] not reproduced here for the sake of clarity. Then, the size phase space is divided into sections and the size distribution function $f(s)$, for which s is the droplet surface, is continuously discretized as

DOI: 10.13009/EUCASS2017-691

a piecewise linear function[26], this method being called *sectional method*. A set of equations is then obtained for each section, and sections are coupled through fluxes. In the vector form, the system of equations for each section (k) is:

$$\begin{cases} \dfrac{\partial \boldsymbol{q}^{(k)}}{\partial t} & + & \boldsymbol{\nabla} \cdot \boldsymbol{f_c}^{(k)} & = & \boldsymbol{s}^{(k)}, \\ \boldsymbol{q}^{(k)} & = & \left(\rho^{(k)} \quad \rho^{(k)} \boldsymbol{w}_d^{(k)} \quad \rho^{(k)} h_d^{(k)} \quad n_d^{(k)}\right)^t, \\ \boldsymbol{f_c}^{(k)} & = & \boldsymbol{q}^{(k)} \otimes \boldsymbol{w}_d^{(k)}, \\ \boldsymbol{s}^{(k)} & = & \boldsymbol{s}_{drag}^{(k)} + \boldsymbol{s}_{rad}^{(k)}, \end{cases} \tag{32}$$

where $\rho^{(k)} = \alpha^{(k)} {\rho_0}^{(k)}$ is the volumetric mass density of droplets with $\alpha^{(k)}$ the local spray volume fraction and ${\rho_0}^{(k)}$ the volumetric mass density of pure liquid, $\boldsymbol{w}_d^{(k)}$ and $h_d^{(k)}$ are respectively the velocity and total energy of all droplets of section (k) located at the position $\boldsymbol{x}$ at time t, and finally $n_d^{(k)}$ is the local number of droplets per unit of volume in the section.

The first source term $\boldsymbol{s}_{drag}^{(k)}$ stands for momentum and energy fluxes between the two solvers due to drag forces. Thanks to the spherical droplets hypothesis made in the spray solver, we can easily calculate the total drag force $\widehat{\boldsymbol{F}}_{drag}^{(k)}$ by integrating the classical expression of the drag force[19] $\boldsymbol{F}_{drag}^{(k)}$ experienced by an isolated droplet over each section (k): $\widehat{\boldsymbol{F}}_{drag}^{(k)} = \int_{s_{k-1}}^{s_k} \boldsymbol{F}_{drag}^{(k)} f(s)\, ds$, where s_{k-1} and s_k are the left and right boundaries of the section (k) respectively. The drag source vector is then expressed as $\boldsymbol{s}_{drag}^{(k)} = \left(0 \quad \widehat{\boldsymbol{F}}_{drag}^{(k)} \quad \widehat{\boldsymbol{F}}_{drag}^{(k)} \cdot \boldsymbol{w}_d^{(k)} \quad 0\right)^t$. The second source term considered in (32) is related to the acoustic radiation force. It is important to note that the coupling between the two solvers only intervene through source terms. Consequently, the ambient fluid does not take into account the volume occupied by the spray and the acoustic field around each spherical droplet is not simulated. As a consequence, the acoustic radiation force experienced by the spray when submitted to a standing wave has to be modelled. The proximity between several droplets may have an impact on this acoustic radiation force. Indeed, it has been demonstrated in the literature[27] that when two or more particles are close enough, there could exist an acoustic interaction force on each droplet due to the scattered waves from the others. According to the authors, this mechanism does not modify the deviation effect in the wave propagation direction observed for isolated particles, but may force the particles to attract or repel each other in the transverse direction. However, as a first approach, it is supposed in this preliminary work that the distance between the spray droplets is sufficiently large to neglect this acoustic interaction force. As a result, it is possible to directly implement the analytical model presented in section 2 (see equation (12)) into the solver to consider the spray deviation under acoustic modulations. The acoustic radiation source term can then be expressed as $\boldsymbol{s}_{rad}^{(k)} = \left(0 \quad n_d^{(k)} \boldsymbol{F}_{rad}^{(k)} \quad n_d^{(k)} \boldsymbol{F}_{rad}^{(k)} \cdot \boldsymbol{w}_d^{(k)} \quad 0\right)^t$ with $\boldsymbol{F}_{rad}^{(k)}$ the acoustic radiation force experienced by every droplets in section (k), evaluated with the mean D_{30} diameter. No integration is performed over the size variable because complementary work showed there are no consequences on the calculation of $\boldsymbol{s}_{rad}^{(k)}$.

Convective fluxes are evaluated through the Godunov's scheme solving the exact Riemann problem at the interface of each mesh cells, with a second-order multislope MUSCL reconstruction[21]. Time integration is performed through a two-step explicit Runge-Kutta scheme.

4. Numerical simulations

4.1 Validation of the acoustic radiation force on a sphere with the Charme solver

As mentioned in the introduction, the long-term objective is to carry out an LES of a subcritical flame under transverse acoustic modulations. In such a case, where the dense liquid core is simulated, the two-phase flow is described by multi-species compressible Navier-Stokes equations. Acoustic waves around this dense liquid core are then directly simulated with a precision depending on both the local spatial discretization and the numerical schemes of the solver, without the need of any specific numerical model. Therefore, to validate the numerical reproduction of acoustic radiation effects on the liquid jet, a fixed rigid sphere of radius a is exposed to a standing acoustic wave at mean atmospheric pressure (see figure 2a). The total acoustic radiation force F_{rad} experienced by the sphere is then compared to the analytical solution derived in section 2. The mesh presented in figure 2b is composed of two different characteristic sizes. The first one Δ_1 has been chosen so that the mesh cut-off frequency is greater than $3f_1$, where f_1 is the second natural mode of the cavity. The second mesh characteristic size Δ_2 has been chosen to have 50 points in one half of the sphere circumference. Acoustics is imposed through pressure fluctuations at the red boundary conditions (see figure 2a). All other boundaries are set to slip wall conditions except for the sphere for which no slip boundary conditions are used.

DOI: 10.13009/EUCASS2017-691

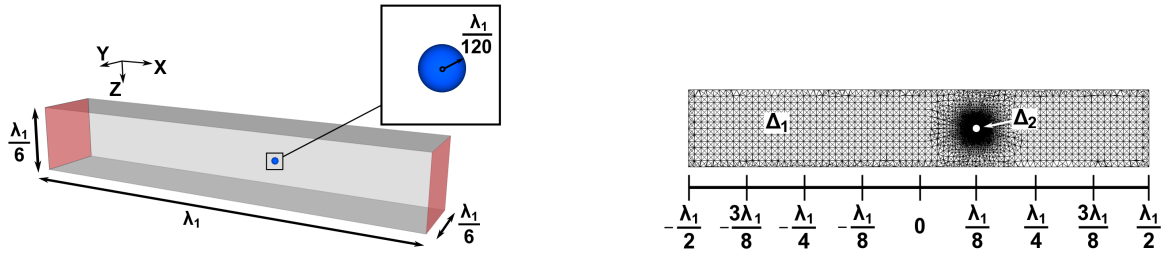

(a) (b)

Figure 2: Numerical geometry (a) and mesh used (b) for the evaluation of the acoustic radiation force experienced by a small and fixed rigid sphere in a transverse acoustic wave.

Mono- and multi-harmonic modulations at low amplitudes

To validate the CHARME solver, two different acoustic modulations are investigated, as defined in table 1 (cases 1 and 2). First, a sinusoidal acoustic modulation is imposed in the cavity at a frequency $f_1 = 1$ kHz corresponding to the second natural frequency of the cavity. For such a modulation, the position of the rigid sphere corresponds to an intensity anti-node (the intensity is defined as the product of pressure and velocity fluctuations). According to King's theory[16], the mean acoustic radiation force is maximum at this location. To ensure a completely linear propagation of waves in the cavity, very low modulation amplitudes are applied. An acoustic level of 130 dB equivalent to a modulation amplitude $P_{ac,1}$ of 89 Pa is imposed based on the commonly used Gol'dberg number[2] Γ, characterizing the strength of non-linear distorsions relative to that of dissipation. The second acoustic modulation is composed of one more harmonic (the third natural mode of the cavity) and is representative of the wave distorsion encountered in non-linear propagation. Amplitude of each acoustic mode is chosen so that the total acoustic energy is the same as for the purely sinusoidal modulation. With reference to the second harmonic, the sphere is located at a velocity anti-node.

Table 1: Acoustic modulation parameters for each simulation. $P_{ac,i}$ is the forcing amplitude of the i^{th} harmonic, f_i its frequency and ψ_i its phase difference with the first harmonic.

$$P'(t) = \sum_{i=1}^{3} P_{ac,i} \sin(2\pi f_i t + \psi_i)$$

	Case 1	**Case 2**	**Case 3**
$P_{ac,1}$ [Pa]	89	87.5	5135
f_1 [Hz]	1000	1000	961
ψ_1 [rad]	0	0	0
$P_{ac,2}$ [Pa]	-	16	887
f_2 [Hz]	-	2000	1922
ψ_2 [rad]	-	0	5.44
$P_{ac,3}$ [Pa]	-	-	555
f_3 [Hz]	-	-	2883
ψ_3 [rad]	-	-	4.97

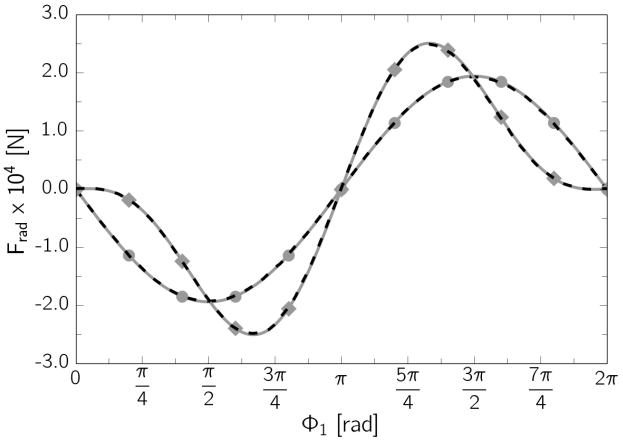

Figure 3: Instantaneous acoustic radiation force experienced by a sphere in a standing acoustic wave. Analytical profiles for case 1 (—●—) and case 2 (—◆—) and corresponding CEDRE results (- - -).

Comparisons between numerical results and the analytical expression of F_{rad} are presented in figure 3 and table 2 over one acoustic period. It can be seen that, for both acoustic modulations, the instantaneous acoustic radiation force is well retrieved by the CEDRE code. In addition, there exists four orders of magnitude between the maximum amplitude of F_{rad} and its mean value. However, it has been proved in section 2 that the effect of these fluctuations $F'_{rad}(t)$ on the sphere deviation could be neglected. As a result, comparisons will be realized only on temporal mean values. For the mono-harmonic modulation, the relative difference between $\langle F_{rad} \rangle$ obtained with CEDRE and the analytical expression is around 8 %. In the multi-harmonic case, this difference only reaches 2 % of the analytical value, which can be considered, in both cases, as sufficiently low to validate the reproduction of the acoustic radiation force with the CHARME solver.

DOI: 10.13009/EUCASS2017-691

In addition, it can be noted that the analytical value obtained from the formulation presented in section 2 correctly degenerates to King's expression (1) for the mono-harmonic modulation ($\langle F_{rad}\rangle_{King}$ = 7.15 x 10^{-8} N). In the multi-harmonic case, this value reaches 6.91 x 10^{-8} N which corresponds to a small relative difference of 3.5 % with the mono-harmonic value. Therefore, in this case, the deviation that could be observed for a mobile sphere would be quasi-identical for both types of modulations. However, it will be shown hereafter that the impact of harmonics on the mean radiation force can be much greater in some cases.

Table 2: Instantaneous and temporal mean acoustic radiation forces on a sphere in a standing wave.

(a)

Case 1		
	Analytical model	Cedre
Amplitude x 10^4 [N]	1.94	1.93
Mean value x 10^8 [N]	7.15	7.75

(b)

Case 2		
	Analytical model	Cedre
Amplitude x 10^4 [N]	2.51	2.49
Mean value x 10^8 [N]	6.91	7.03

Multi-harmonic modulation at higher amplitudes

At this point, the objective beyond the scope of the preliminary work presented in this paper should be explained: carrying out an LES reproducing an experimental air-assisted jet submitted to high frequency/high amplitude acoustic modulations[4] in order to investigate the coupling between acoustics and the two-phase flow. For this reason, it is interesting to reproduce the previous test case with an acoustic modulation representative of the one imposed in experiments of Baillot *et al*.[4] An FFT of the raw experimental acoustic signal indicates that more than 99.8 % of the acoustic energy is comprised into the frequency range [0 Hz ; 3 000 Hz] and more precisely in the second, third and fourth natural modes of the cavity. To numerically reproduce this acoustic modulation, it is then possible to reconstruct this signal by considering only these three harmonics. The experimental signal is plotted on figure 4 together with its reconstruction used for the numerical acoustic modulation. Parameters used for this numerical reconstruction are presented in table 1 (case 3).

The acoustic radiation force experienced by the sphere once submitted to this acoustic modulation is shown in figure 5 over one acoustic period and numerical values are presented in table 3. First, these results demonstrate the ability of the Charme solver to correctly reproduce the dramatic effect of all harmonics on the shape of the instantaneous profile of F_{rad}. However, as explained before, the parameter of interest is the temporal mean value $\langle F_{rad}\rangle$. In this case, the relative difference between the numerical and analytical mean acoustic radiation forces is only about 3 % of the analytical value, which validates the solver in presence of high amplitude acoustic modulations.

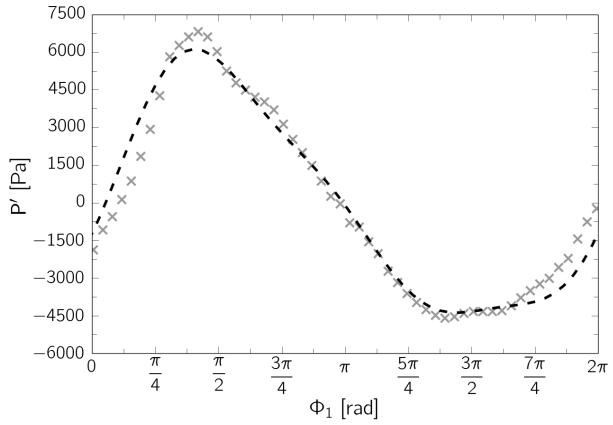

Figure 4: Raw experimental acoustic signal of Baillot *et al*. (×) and its numerical reconstruction based on the frequency range [0 Hz ; 3 000 Hz](- - -).

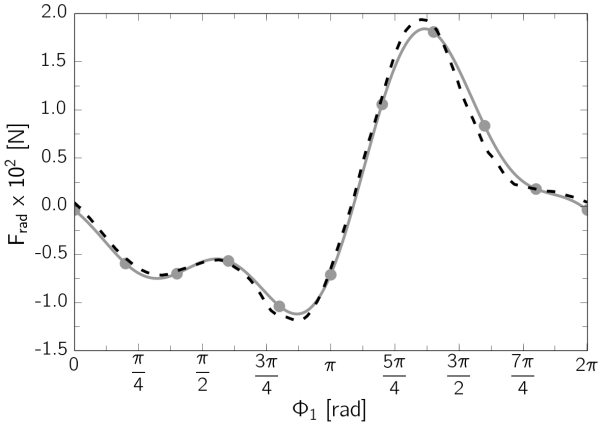

Figure 5: Acoustic radiation force experienced by a sphere in a standing acoustic wave. Analytical profile for case 3 (—●—) and corresponding Cedre results (- - -).

As done before for low amplitude cases, we can easily compare the value of the mean acoustic radiation force given by King's model taking into account only one harmonic ($\langle F_{rad}\rangle_{King}$ = 2.30 x 10^{-4} N) and the one announced by the analytical model presented in section 2, which takes into account the presence of multiple harmonics. In this case,

DOI: 10.13009/EUCASS2017-691

Table 3: Instantaneous and temporal mean acoustic radiation forces on a sphere in a standing wave.

Case 3		
	Analytical model	CEDRE
Amplitude x 10^2 [N]	1.84	1.93
Mean value x 10^4 [N]	2.21	2.14

the relative difference only reaches 4 % of the value predicted by the updated model. As for low amplitudes, the impact of harmonics on the mean acoustic radiation force is then very low at this location in the acoustic field. However, by plotting $\langle F_{rad} \rangle$ over the wave propagation axis for both models (see figure 6), we can see that this relative difference can rise up to 60 % at the intensity anti-node located at X = $3\lambda_1/8$. This result demonstrates the importance of considering the presence of multiple harmonics when evaluating the acoustic radiation force and its effects on any object submitted to high amplitude standing waves.

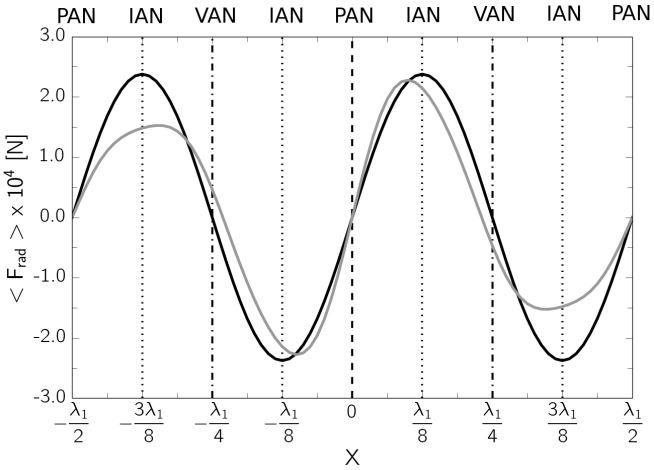

Figure 6: Mean acoustic radiation force experienced by a sphere for different locations on the wave propagation axis. King's model for mono-harmonic waves (—). Updated model adapted to multi-harmonic waves (—).

4.2 Application of the updated model to the SPIREE solver

We are interested here in investigating step by step the deviation of droplets under high amplitude multi-harmonic acoustic modulations. In air-assisted jets submitted to acoustics, the force experienced by the spray droplets can be decomposed into two components as mentioned in section 3: a first one due to the drag force between droplets and the coaxial gaseous flow and a second one due to the acoustic radiation force. Gravity is neglected here because preliminary work showed it has no impact on the spray dynamics. To investigate the impact of each component on the spray deviation, two different situations are investigated: a first one where the acoustic radiation force is isolated and a second one where drag is considered. The numerical configuration and the associated mesh are represented in figure 7a and 7b respectively. The mesh is composed of a far field zone adapted to acoustic propagation and a second zone with finer cell size adapted to the spray discretization. The mesh parameter Δ_1 adapted to the acoustic propagation has been chosen with the same criteria as for the test case presented in section 4.1. Droplets of two different diameters $D_1 = 2a_1 = 20$ µm and $D_2 = 2a_2 = 250$ µm are injected with an initial vertical velocity $V_{p,inj} = 1\,\mathrm{m \cdot s^{-1}}$ in a cavity. As explained in section 3, a specific model has been integrated to the SPIREE solver in order to simulate the effect of acoustics on the spray dynamics. By activating this model, the droplets can experience an acoustic radiation force oriented towards the closest velocity anti-node without the need of any acoustic modulation in the CHARME solver. It is however necessary to indicate the acoustic modulation parameters to the SPIREE solver. For the two situations presented below, these parameters correspond to the ones used in case 3 of section 4.1 (see table 1).

Acoustic radiation effect on droplets trajectories

First, in order to isolate the effect of the acoustic radiation force on droplets trajectories, the F_{rad} model is

DOI: 10.13009/EUCASS2017-691

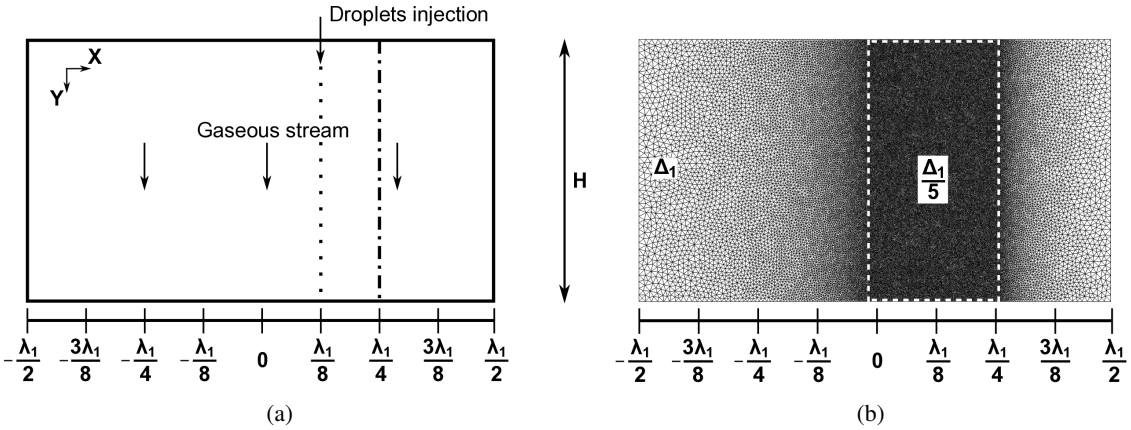

Figure 7: Numerical geometry (a) and mesh (b) to investigate a spray deviation when submitted to acoustics. Acoustics is imposed only through the F_{rad} model in the Spiree solver. The top and bottom boundary conditions are respectively inlet and outlet. Intensity anti-node (⋯⋯) and velocity anti-node (▬·▬) for the first harmonic.

activated in the Spiree solver without drag between the droplets and the ambient gas. Therefore, the only non null source term in the system of equation (32) is s_{rad}. The resulting mean trajectories for the two types of droplets are represented in figure 8. In this situation, both types of droplets are deviated to the nearest velocity anti-node, as predicted by the theory. Regarding the comparison between behaviours of both droplets sizes, King's theory predicts an evolution of the type $F_{rad} \propto a^3$ for small droplets (see equation (1)). This can be proved in the same way for multi-harmonic waves. However, despite the fact that the droplets injected in this numerical simulation can be considered small enough compared to the acoustic wave length of each harmonic ($k_3 a_2 = 6.5 \times 10^{-3} \ll 1$), it can be seen from figure 8 that both trajectories are identical. This is due to droplets inertia. Indeed, the equation of motion (30) clearly shows that the greater its mass is, the less a droplet accelerates under a given acoustic radiation force. Since $M \propto a^3$, it is natural to find exactly the same trajectories for both types of droplets.

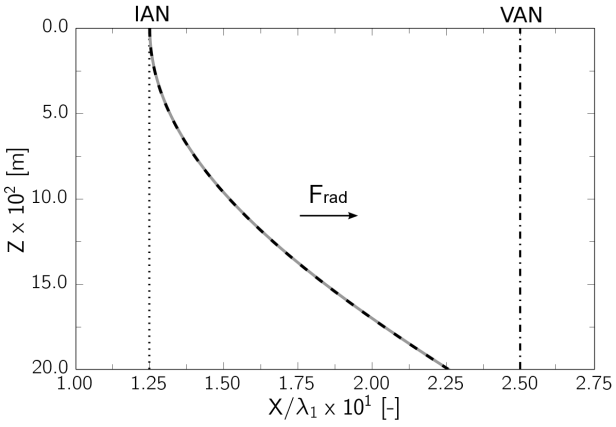

Figure 8: Zoom on the mean trajectories of 20 µm (▬) and 250 µm (▬ ▬) droplets submitted to acoustic radiation force without drag. Intensity anti-node (vertical ⋯⋯) and velocity anti-node (vertical ▬·▬) for the first harmonic.

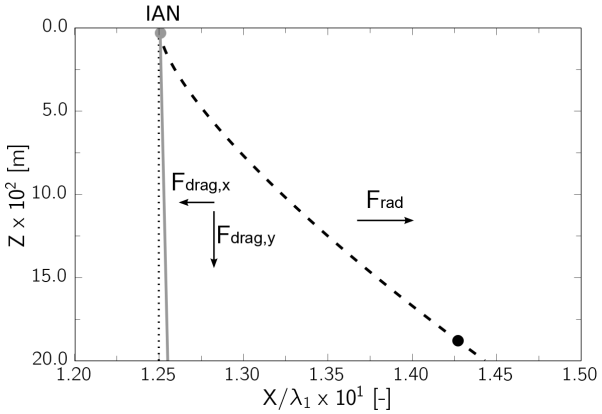

Figure 9: Zoom on the mean trajectories of 20 µm (▬) and 250 µm (▬ ▬) droplets submitted to acoustic radiation force and a homogeneous and constant vertical flow with drag. Intensity anti-node (vertical ⋯⋯) for the first harmonic. The two points represent the locations where $V_p = 0.9 V_g$ for both droplet diameters.

Vertical flow effect on droplets trajectories

The second situation corresponds to droplets submitted to the acoustic radiation force and drag. A homogeneous and constant gaseous flow with velocity $\boldsymbol{V}_g = 3\boldsymbol{V}_{p,inj}$ is simulated to get closer to what happens downstream atomization processes in coaxial two-phase flows. To investigate the part played by this mean flow on droplets deviation, the drag source term in the system of equation (32) is activated in the Spiree solver. The resulting mean trajectories for

DOI: 10.13009/EUCASS2017-691

the two types of droplets are represented in figure 9. In this situation, the droplets are still deviated toward the nearest velocity anti-node, as expected, but with lower amplitudes. Indeed, now that drag is taken into account, each droplet experiences an additional force $\boldsymbol{F}_{drag}$ due to the momentum transfer with the gaseous stream. This force can be divided into two components $\boldsymbol{F}_{drag,x}$ and $\boldsymbol{F}_{drag,y}$, as represented on figure 9, and can be expressed as:

$$\boldsymbol{F}_{drag} = \underbrace{M\frac{u-\dot{\xi}}{\tau}\,\vec{X}}_{\boldsymbol{F}_{drag,x}} + \underbrace{M\frac{v-\dot{\eta}}{\tau}\,\vec{Y}}_{\boldsymbol{F}_{drag,y}}, \tag{33}$$

where $(u,\ v)$ and $(\dot{\xi},\ \dot{\eta})$ are the gas and droplet velocities respectively, τ is the characteristic response time of the droplet and M its mass. For the situation investigated here, $\boldsymbol{F}_{drag,x}$ is oriented to the opposite direction of F_{rad}, which tends to reduce the droplets acceleration in the horizontal direction, while $\boldsymbol{F}_{drag,y}$ tends to accelerate them in the vertical direction because of the presence of the imposed gaseous flow. The result of these two additional forces is a dramatic reduction of the deviation for both types of droplets compared to the previous situation without drag. It can also be noticed a great difference between the dynamics of small and bigger droplets. The Stokes number, directly related to the characteristic response time as $St_i = \tau_i\ V_g/a_i$, is much greater for the bigger droplets than for the smaller ones ($St_1 \approx 140 \ll St_2 \approx 860$). Therefore, smaller droplets of diameter $D_1 = 20$ µm reach the gas velocity faster than bigger particles of diameter $D_2 = 250$ µm and experience consequently a lower deviation. This phenomenon is represented on figure 9 with two points located at the positions where the droplet velocity reaches 90 % of the gaseous one. To conclude, both the acoustic radiation force and the drag have a great impact on the deviation of polydisperse sprays submitted to transverse acoustics and can induce an important size segregation. This phenomenon may play a part in the triggering of combustion instabilities in liquid rocket engines at subcritical operating conditions.

5. Conclusion

In this paper, we present a preliminary work on the numerical investigation of acoustic radiation effects on coaxial two-phase flows. First, a new analytical formulation of the acoustic radiation force experienced by a sphere submitted to a high frequency / high amplitude standing acoustic wave is developed. Based on King's initial theory adapted to mono-harmonic acoustic waves, this updated formulation brings the possibility to consider the effect of multiple harmonics and their coupling, which is more representative of what can be observed in Liquid Rocket Engines (LRE). The importance to take into account the presence of such harmonics is then underlined through several numerical simulations of a fixed rigid sphere under acoustic modulations. These simulations are also the occasion to validate the ability of the *separated phase* solver to reproduce the acoustic radiation force on an object, which plays an important part in the behaviour of the dense liquid core observed in excited two-phase flows.

To simulate the spray resulting from the atomisation of such liquid core, we use a different solver based on a Eulerian statistical approach. With this solver, the acoustic radiation force experienced by the droplets of the spray cannot be simulated and has to be modelled. As a first approach, the possible interaction effect between the droplets is neglected and the updated analytical formulation of the acoustic radiation force adapted to multi-harmonic waves is implemented. Finally, thanks to this new model, the dynamics of a polydisperse spray under acoustic modulations is progressively investigated. First, it is demonstrated that, when drag is not considered, the acoustic radiation force induces an identical deviation of all droplets as long as their size can be considered small enough compared to the acoustic wave length. Once drag is taken into account, it is shown that bigger droplets will experience a much greater deviation than smaller ones. This size segregation may play an important role in the triggering of combustion instabilities in LRE operating at subcritical conditions.

On-going work is carried out to investigate acoustic radiation effects on a full air-assisted jet. A practical configuration[11] will be simulated with the Cedre code and the numerical results will be compared to experimental data. For this purpose, an additional effort is required to assure a correct coupling between the *separated phase* and the spray solvers once the radiation force model is activated. This simulation is the last step of the validation procedure of the Cedre code and will be the occasion to investigate acoustic radiation effects in more realistic operating conditions.

6. Acknowledgments

This work is supported and co-supervised by Cnes the French Space Agency. We gratefully thank CORIA for sharing their experience. The on-going work will be the occasion to maintain the joint effort between both labs. This work was granted access to the high-performance computing resources of CINES made available by Grand Equipement National de Calcul Intensif (Genci) under the allocation A0022B07710.

DOI: 10.13009/EUCASS2017-691

References

[1] Anderson, W. E. and Yang, V. Liquid Rocket Engine Combustion Instability. *Progress in Astronautics and Aeronautics*, 1995.

[2] Baars, W. J., Tinney, C. E., Wochner, M. S. and Hamilton, M. F. On cumulative nonlinear acoustic waveform distortions from high-speed jets. *Journal of Fluid Mechanics*, 749:331–366, 2014.

[3] Baillot, F., Blaisot, J.-B., Boisdron, G. and Dumouchel, C. Behaviour of an air-assisted jet submitted to a transverse high-frequency acoustic field. *Journal of Fluid Mechanics*, 640:305–342, 2009.

[4] Baillot, F., Blaisot, J.-B., Richard, C. and Théron, M. Effects of acoustic radiation on air-assisted jets in a transverse high-frequency acoustic field. In *25th ILASS Conference*, 2013.

[5] Buffum, F.G. and Williams, F.A. The Response of a Turbulent Liquid Jet to Transverse Acoustic Fields. *Proceedings of the 1967 Heat Transfer and Fluid Mechanics Institute*, 247–276, 1967.

[6] Chehroudi, B. and Talley, D. Interaction of acoustic waves with a cryogenic nitrogen jet at sub- and supercritical pressures. In *40th AIAA Aerospace Sciences Meeting & Exhibit*, 2002.

[7] Chehroudi, B., Davis, D. and Talley, D. The Effects of Pressure and Acoustic Field on a Cryogenic Coaxial Jet. In *42th AIAA Aerospace Sciences Meeting & Exhibit*, 2004.

[8] Culick, F. E. C. Unsteady Motions in Combustion Chambers for Propulsion Systems, 2006.

[9] Davis, D. and Chehroudi, B. Shear-Coaxial Jets from a Rocket-Like Injector in a Transverse Acoustic Field at High Pressures. In *44th AIAA Aerospace Sciences Meeting & Exhibit*, 2006.

[10] Davis, D. and Chehroudi, B. Measurements in an Acoustically Driven Coaxial Jet under Sub-, Near-, and Supercritical Conditions. *Journal of Propulsion and Power*, 23(2):364–374, 2007.

[11] Ficuciello, A., Baillot, F., Blaisot, J.-B., Richard, C. and Théron, M. High Amplitude Acoustic Field Effects on Air-Assisted Liquid Jet. In *52nd AIAA/SAE/ASEE Joint Propulsion Conference*, 2016.

[12] Hakim, L., Schmitt, T., Ducruix, S. and Candel, S. Dynamics of a transcritical coaxial flame under a high-frequency transverse acoustic forcing: Influence of the modulation frequency on the flame response. *Combustion and Flame*, 162:3482–3502, 2015.

[13] Hakim, L., Ruiz, A., Schmitt, T., Boileau, M., Staffelbach, G., Ducruix, S., Cuenot, B. and Candel, S. Large eddy simulations of multiple transcritical coaxial flames submitted to a high-frequency transverse acoustic modulation. *Proceedings of the Combustion Institute*, 35(2):1461–1468, 2015.

[14] Harrje, D. T. and Reardon, F. H. Liquid propellant rocket combustion instability. NASA S.P. 194, 1972.

[15] Hoover, D.V., Ryan, H.M., Pal, S., Merkle, C.L., Jacobs, H.R. and Santoro, R.J. Pressure Oscillation Effects on Jet Breakup. *Heat and Mass Transfer in Spray Systems*, 187:27-36, 1991.

[16] King, L.V. On the Acoustic Radiation Pressure on Spheres. *Proceedings of the Royal Society A: Mathematical, Physical and Engineering Sciences*, 147(861):212–240, 1934.

[17] Laurent, F. and Massot, M. Multi-fluid modelling of laminar polydisperse spray flames: origin, assumptions and comparison of sectional and sampling methods. *Combustion Theory and Modelling*, 5:537–572, 2001.

[18] Leung, E., Jacobi, N. and Wang, T. Acoustic radiation force on a rigid sphere in a resonance chamber. *The Journal of the Acoustical Society of America*, 70(6):1762–1767, 1981.

[19] Le Touze, C. Couplage entre modèles diphasiques à « phases séparées » et à « phase dispersée » pour la simulation de l'atomisation primaire en combustion cryotechnique. PhD thesis, Université Nice Sophia Antipolis, 2015.

[20] Le Touze, C., Murrone, A. and Montreuil, E. Numerical coupling strategies for the "separated-to-dispersed" transition within the liquid phase of cryogenic rocket engines. In *5th EUCASS Conference*. Germany, 2013.

[21] Le Touze, C., Murrone, A. and Guillard, H. Multislope MUSCL method for general unstructured meshes. *Journal of Computational Physics*, 284:389–418, 2015.

[22] Lierke, E.G., Grossbach, R., Flogel, K. and Clancy, P. Acoustic Positioning for Space Processing of Materials Science Samples in Mirror Furnaces. In *ULTRASONICS SYMPOSIUM*, 1129–1139, 1983.

[23] Miesse, C.C. The Effect of Ambient Pressure Oscillations on the Disintegration and Dispersion of a Liquid Jet. *Journal of Jet Propulsion*, 25(10):525–530, 1955.

[24] Oefelein, J. C. and Yang, V. Comprehensive Review of Liquid-Propellant Combustion Instabilities in F-1 Engines. *Journal of Propulsion and Power*, 9:657–677, 1993.

[25] Refloch, A. Cedre Software. *AerospaceLab Journal*, Issue 2, March 2011.

[26] Sibra, A., Dupays, J., Murrone, A., Laurent, F. and Massot, M. Simulation of reactive polydisperse sprays strongly coupled to unsteady flows in solid rocket motors: Efficient strategy using Eulerian Multi-Fluid methods. *Journal of Computational Physics*, 339:210–246, 2016.

[27] Silva, G. T. and Bruus, H. Acoustic interaction forces between small particles in an ideal fluid. *Physical Review E*, 90(6), 2014.

[28] Toro, E.F., Spruce, M. and Speares, W. Restoration of the contact surface in the HLL-Riemann solver. *Shock Waves*, 4(1):25–34, 1994.

[29] Urbano, A., Selle, L., Staffelbach, G., Cuenot, B., Schmitt, T., Ducruix, S. and Candel, S. Exploration of combustion instability triggering using Large Eddy Simulation of a multiple injector liquid rocket engine. *Combustion and Flame*, 169:129–140, 2016.

[30] Vingert, L., Habiballah, M. and Traineau, J.C. MASCOTTE : a research test facility for high pressure combustion of cryogenic propellants. In *12th European Aerospace Conference*. Paris, 1999.

[31] Williams, F. A. Spray Combustion and Atomization. *Physics of Fluids*, 1:541–546, 1958.